



LAWRENCE
LIVERMORE
NATIONAL
LABORATORY

Improving the off-axis spatial resolution and dynamic range of the NIF X-ray streak cameras

A. G. MacPhee, A. K. L. Dymoke-Bradshaw, J. D. Hares, J. Hassett, B. W. Hatch, A. L. Meadowcroft, P. M. Bell, D. K. Bradley, P. S. Datte, O. L. Landen, N. E. Palmer, K. W. Piston, V. V. Rekow, T. J. Hilsabeck, J. D.ilkenny

June 7, 2016

HTPD 2016
Madison, WI, United States
June 5, 2016 through June 9, 2016

Disclaimer

This document was prepared as an account of work sponsored by an agency of the United States government. Neither the United States government nor Lawrence Livermore National Security, LLC, nor any of their employees makes any warranty, expressed or implied, or assumes any legal liability or responsibility for the accuracy, completeness, or usefulness of any information, apparatus, product, or process disclosed, or represents that its use would not infringe privately owned rights. Reference herein to any specific commercial product, process, or service by trade name, trademark, manufacturer, or otherwise does not necessarily constitute or imply its endorsement, recommendation, or favoring by the United States government or Lawrence Livermore National Security, LLC. The views and opinions of authors expressed herein do not necessarily state or reflect those of the United States government or Lawrence Livermore National Security, LLC, and shall not be used for advertising or product endorsement purposes.

Improving the off-axis spatial resolution and dynamic range of the NIF X-ray streak cameras^{a)}

A. G. MacPhee^{1, b)}, A. K. L. Dymoke-Bradshaw³, J. D. Hares³, J. Hassett^{1,2}, B. W. Hatch, A. L. Meadowcroft⁴, P. M. Bell¹, D. K. Bradley¹, P. S. Datte¹, O. L. Landen¹, N. E. Palmer¹, K. W. Piston¹, V. V. Rekow¹, T. J. Hilsabeck⁵, J. D. Kilkenny⁵

¹Lawrence Livermore National Laboratory, P.O. Box 808, Livermore, California 94551-0808, USA

²Department of Electrical and Computer Engineering, University of Rochester, Rochester, New York 14627, USA

³Kentech Instruments Ltd., Isis Building, Howbery Park, Wallingford, Oxfordshire, OX10 8BD, UK

⁴AWE Aldermaston, Reading, Berkshire, RG7 4PR, UK

⁵General Atomics, P.O. Box 85608, San Diego, California 92186-5608, USA

(Presented 080816; received XXXXX; accepted XXXXX; published online XXXXX)

(Dates appearing here are provided by the Editorial Office)

We report simulations and experiments that demonstrate an increase in spatial resolution of the NIF core diagnostic x-ray streak cameras by a factor of two, especially off axis. A design was achieved by using a corrector electron optic to flatten the field curvature at the detector plane and corroborated by measurement. In addition, particle in cell simulations were performed to identify the regions in the streak camera that contribute most to space charge blurring. These simulations provide a tool for convolving synthetic pre-shot spectra with the instrument function so signal levels can be set to maximize dynamic range for the relevant part of the streak record.

I. INTRODUCTION

There are several x-ray streak cameras in use at Lawrence Livermore National Laboratory's National Ignition Facility (NIF)¹. Figure 1 shows a streak measuring the implosion of the limbs of a shell on the NIF². The existing streak cameras provide about five resolution elements across the shadow of each limb. It is desirable to have more resolution elements across the limb to enable a more precise measure of the shell density profile from which the remaining shell mass as a function of time can be inferred.

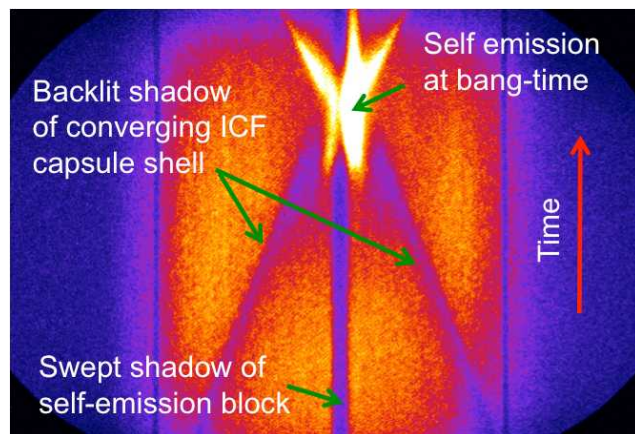


Figure 1 Streaked radiograph of an ICF capsule

As the region of interest moves across the field of view as a function of time, increasing the magnification would eliminate a portion of the record; hence to improve the limb resolution while maintaining field of view, the number of simultaneously swept channels must be increased. Moreover, once the capsule

converges at *bang time*, a bright flash of X-ray self-emission occurs. Although partially blocked by the shadow of a thin wire on axis, significant space charge broadening results, which can perturb the record both locally and globally, thus limiting the useful dynamic range of the entire streak record.

The Kentech Instruments Low-Magnification streak tube³ on which the NIF core diagnostics x-ray streak cameras are based is shown in figure 2. The one-dimensional slit electron source object formed at a flat photocathode by the incident x-ray signal is relayed onto a flat, two-dimensional electron detector by the electron optics. Deflection plates behind the anode aperture sweep the electron slit image across the detector, giving a record of the temporal variation of the X-ray signal along the slit as a function of time.

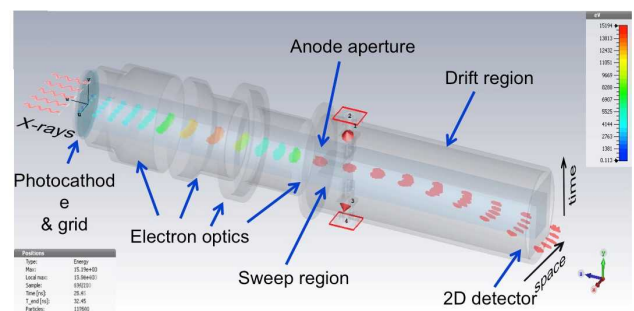


Figure 2 A snapshot from a particle in cell simulation of the Kentech streak tube used to evaluate space charge effects. Electron energy is indicated by the color bar.

The electron optics in this existing design comprise a three-element *immersion lens* followed by a diverging *aperture lens*.

^{a)}Invited paper published as part of the Proceedings of the 21st Topical Conference on High-Temperature Plasma Diagnostics (HTPD 2016) in Madison, Wisconsin, USA.

^{b)}Author to whom correspondence should be addressed: macphee2@llnl.gov

An immersion lens has multiple elements at different potential, analogous to an optical lens comprising materials with different refractive indices. An aperture lens is formed by the hole in the anode aperture electrode separating two regions with differing axial field. As in the case for visible optics the imaging properties of successive electron optic lens elements can be described using matrices and combined into a single transfer matrix (see for example⁴). Corresponding electron optic aberrations follow in a similar way: the aberrations of concern here are Petzval field curvature⁵ and to a lesser extent spherical aberration.

In this paper we describe a reduction in field curvature leading to at least a twofold increase in spatial resolution for the NIF x-ray streak cameras. Guided by electron optic simulations using the software package Simion⁶, we designed and experimentally tested two methods for reducing field curvature; one of which also improved spatial resolution and spherical aberration and under certain circumstances may have the potential to increase dynamic range. Using the commercial software package CST Particle Studio (PS)⁷, we have developed a numerical model of the instrument response function to identify regions in the camera most susceptible to space charge effects. PS uses a time domain 3D PIC solver based on the code MAFIA^{8,9} developed since the 1970's for designing particle accelerators. It uses the finite integration technique in a leapfrog algorithm to produce fully consistent simulations of relativistic charged particles in both static and dynamic electromagnetic fields. Using this model, signal attenuation can now be set based on the convolution of predicted spectra with the instrument response, paying particular attention to the features of interest rather than a more conservative generic saturation limit, allowing fuller use of the available dynamic range.

II. FIELD CURVATURE SIMULATIONS

Field curvature for visible optics close to the optic axis is approximately spherical, with radius r_p given by the Petzval sum⁵ as shown in figure 3, for k spherical surfaces with radii r_i and refractive indices n_i and n_i^* , for inbound and outbound rays respectively.

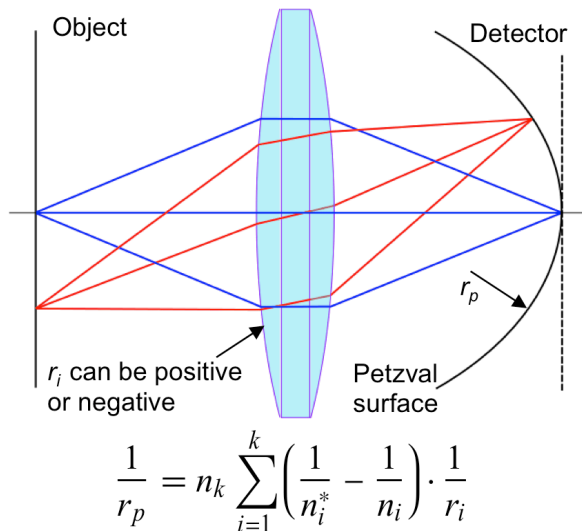


Figure 3 Petzval field curvature in photon optics

The Petzval sum can be recast for electron optics in a similar form¹⁰ illustrated in figure 4. Here we have used Simion⁶ to solve Laplace's equation for the electrostatic field of the cylindrically symmetric streak converter tube with standard electron optics and traced the resulting electron trajectories, then mapped out the Petzval surface by calculating the position of the spatial minima for the 3D electron trajectories for each bundle of rays leaving a series of point along the photocathode.

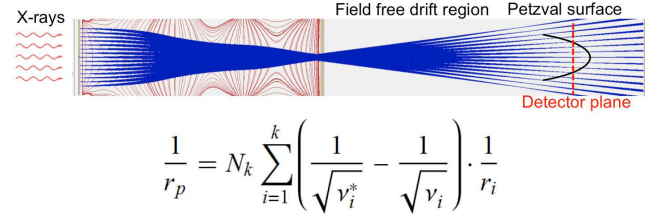


Figure 4 Petzval field curvature in electron optics

Here $v = V_i / V_k$ at each equipotential surface (red lines) from surfaces i through k , and $*$ denotes the outbound side of the surface. Figure 5 shows details at the detector plane.

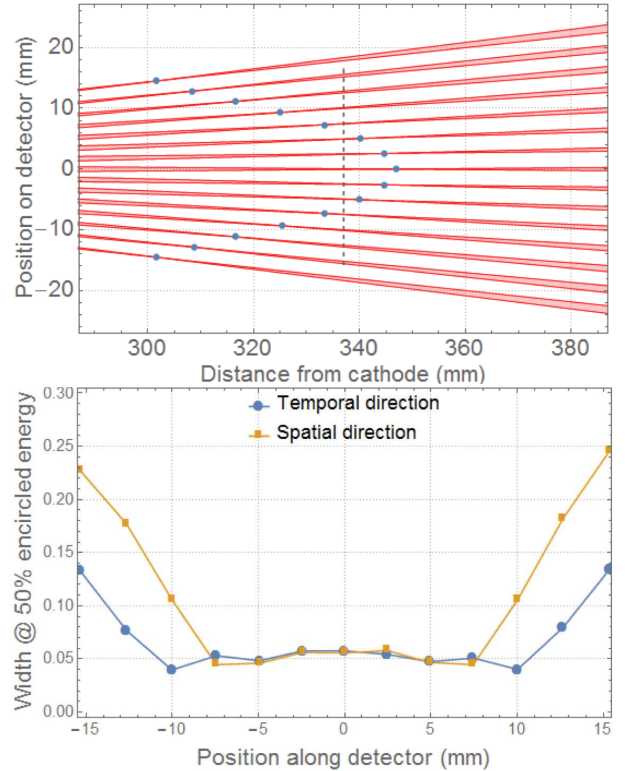


Figure 5 Cross-section through the Petzval surface at the detector plane for the standard optics solved by ray-tracing. Spot width measured in the spatial direction is of most concern here as the temporal slit width is usually of the order $\sim 250\mu\text{m}$

The standard electron optics paired with a flat detector severely limit the number or resolution elements and the curvature is sufficiently tight that a curved fiber optic plus phosphor would be close to grazing only a little way off axis. Clearly we need to explore options that reduce the Petzval sum. A new insight of this work is the defocusing effect of the anode

aperture is illustrated in figure 6. For the approximation of a thin aperture, it can be shown that the focal length is equal to four times the distance between the aperture and the first flat equipotential¹¹, which in this case is ~15mm. This is the strongest lens in the system, with the highest field gradient outside of the extraction region, and therefore presents the most significant contribution to the Petzval sum.

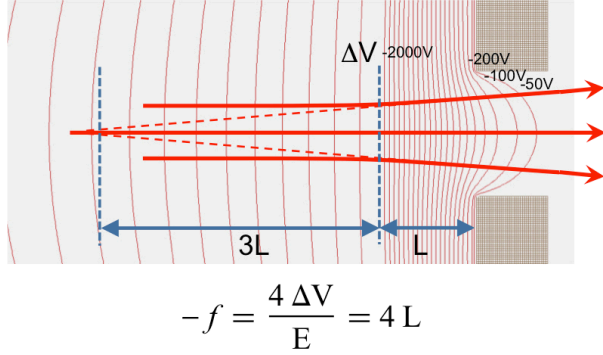


Figure 6 The focal length of a diverging aperture lens

The first solution for reducing field curvature is then to eliminate the negative lens associated with the anode aperture. This can be achieved by covering the aperture with a thin conducting foil, or more practically a mesh, as a sub-micron foil would not survive the vacuum environment. With the curved equipotentials in the vicinity of the anode aperture eliminated, the solution for the tube potential results in a more favorable Petzval surface as shown in figure 7:

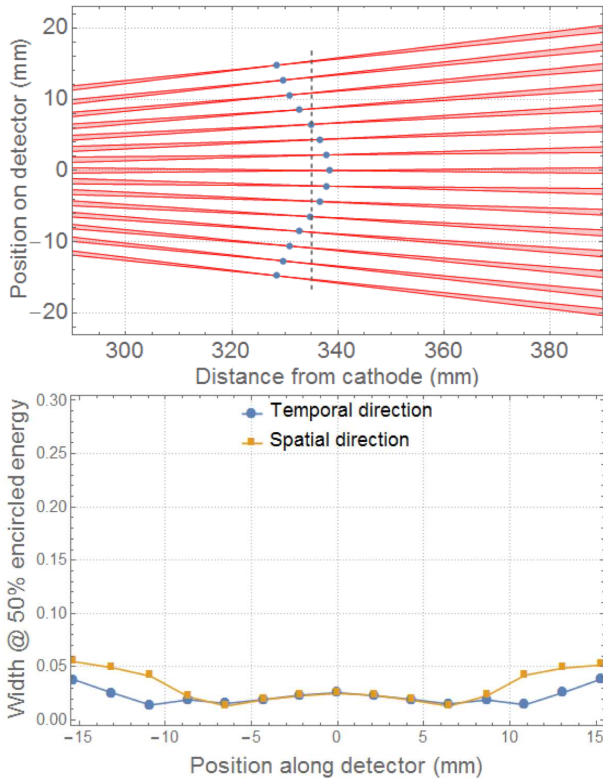


Figure 7 Eliminating the lens associated with the anode aperture significantly reduces Petzval curvature

The second and better approach to reducing the Petzval sum was to design a corrector lens. Optical correctors for field curvature employ a series of meniscus lenses. The electron optic equivalent can be formed using the fringing field around the lip of a cylinder, combined with a mesh to flatten the equipotentials on axis as shown in figure 8.

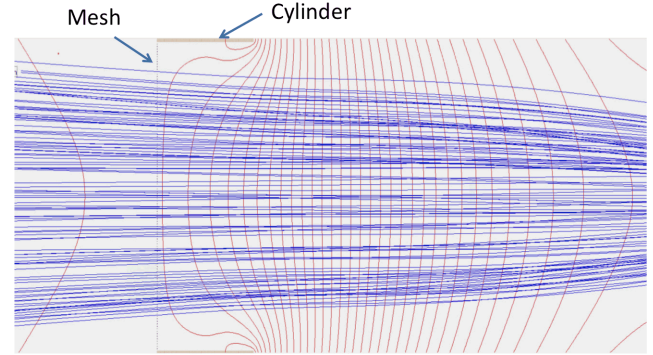


Figure 8 Implementing a negative component to the Petzval sum

The resulting Petzval surface and detector plane cross-section are shown in figure 9.

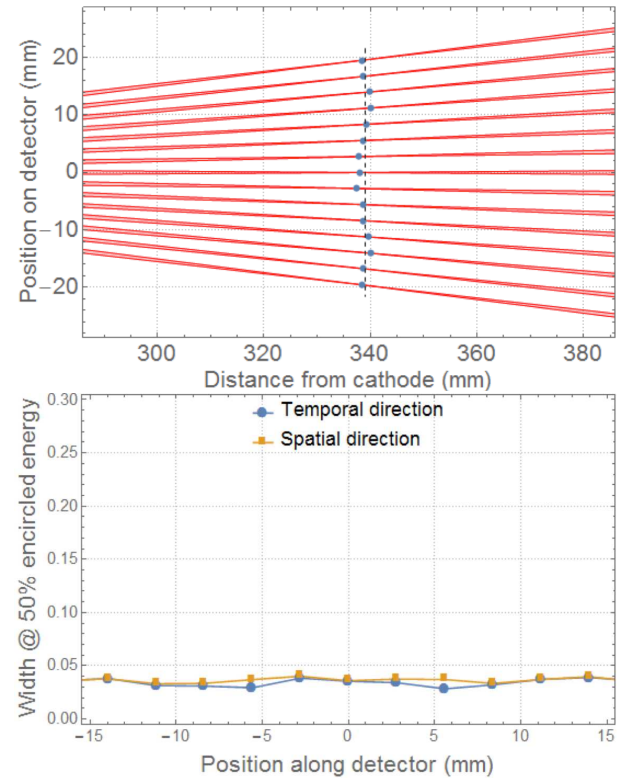


Figure 9 Petzval surface and cross-section through detector plane using the corrector optic

III. RESOLUTION MEASUREMENTS

To evaluate the performance of the correction techniques we recorded electron images using the streak tube with a resolution

test chart photocathode exposed to a UV mercury discharge lamp. The detector was an electron bombarded 2k x 512 back illuminated CCD with 13.5 μ m square pixels for an image area $\sim 26 \times 6 \text{ mm}^2$. The camera was mounted on an offset flange to record a little over half of the symmetrical electron image. Figure 10 shows the data recorded, with the circle in the test pattern on the axis of the image tube.

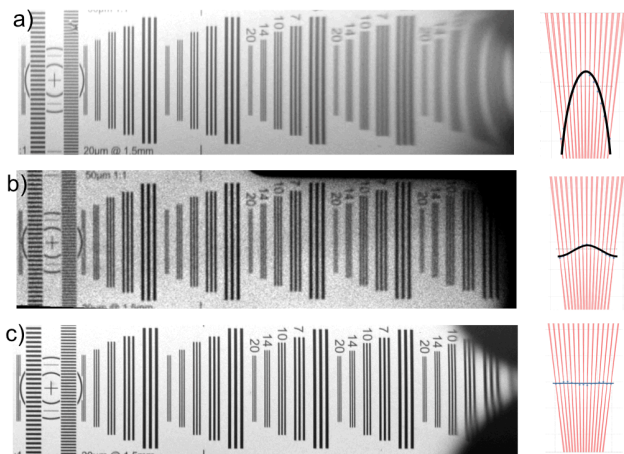


Figure 10 Resolution chart data recorded for a) standard optics, b) 500 lp/mm mesh over aperture, c) with corrector lens. The left side of the charts are on axis; the right side of the charts are 15mm off axis. There is imperceptible degradation for case c 15mm off axis on the right.

The test pattern data recorded in figure 10 was used to construct the modulation transfer function (MTF) plots in figure 11 (mesh aperture scheme) and figure 12 (corrector lens scheme). In both plots the MTF curve for the standard optics is shown in the background with semi-transparent squares for reference.

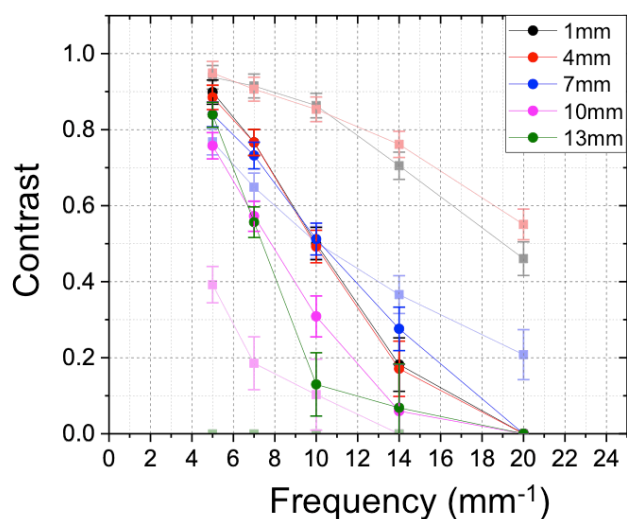


Figure 11 MTF curves for the mesh/aperture scheme at a range of off-axis distances

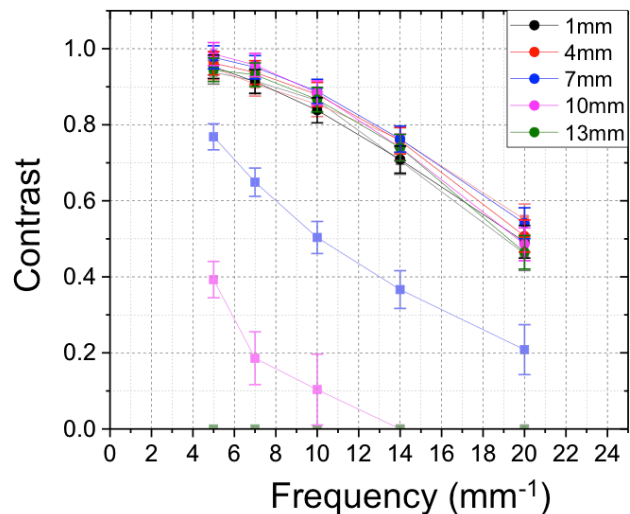


Figure 12 MTF curves for the Petzval corrector scheme at a range of off-axis distances

The experimental data show clearly that Petzval field curvature has been reduced in both cases; the contrast being greater at 10mm and 13mm off-axis compared to the standard optics. For the mesh/aperture case however, contrast is in general reduced at all frequencies. This is attributable to the array of rectangular *facet lenses* formed by the mesh and has been studied in detail for spherical meshes in the reduction of spherical aberrations in photoelectron spectroscopy¹³. In the present case we observed an improvement in resolution by changing the mesh pitch from 100 lp / mm to the plotted MTF with 500 lp / mm, but no further improvement at 750 lp / mm. The corrector lens scheme on the other hand maintains the same on axis resolution of the standard optics out to the full 13mm off-axis radius accessible, despite this scheme also employing a 500 lp / mm mesh. In this case the potential gradient adjacent to the mesh is 5x lower than with the mesh installed over the anode aperture, $\sim 100 \text{ V/mm}$ vs. 500 V/mm , significantly reducing the strength of the individual facet lens elements. In general the MTF data does not suggest further improvement in contrast at higher frequencies due to a reduction in spherical aberration suggested by ray-tracing although this may have been masked by residual blurring due to the mesh.

IV. RELEVANCE TO X-RAY MEASUREMENT

The resolution data reported here used a gold photocathode excited by UV light from a mercury vapor discharge lamp. It is well known that the energy distribution of electrons from typical X-ray photocathode materials varies significantly¹⁴. We currently have no resolution test chart for X-rays, although one is planned. We have measured the width of the line spread function obtained for the streak tube using a 20 μ m slit with both a gold and a CsI photocathode exposed to UV at 4.89eV and Ni-K α X-rays at 7.5keV. In all cases the measurements were near the limit of the recording resolution at $\sim 30 \mu\text{m}$ fwhm, except for gold excited by X-rays which had fwhm $\sim 40 \mu\text{m}$. Given the significantly broader secondary electron energy distribution from gold when excited by x-rays, this is to be expected, and simply ray-tracing the same optics using a higher electron starting energy required $\sim 3 \text{ eV}$ to increase the fwhm to $\sim 40 \mu\text{m}$, which is significantly greater than the average energy from gold and more so compared to CsI and KBr. The energy distribution from CsI under X-ray excitation¹⁴ is similar to that for gold under UV excitation¹⁵, as shown in figure 13. This is attributed to impurities in the gold exposed to air

reducing the work function to $\sim 3.7\text{eV}$. Combined with our line spread function width measurements this gives confidence that our planned MTF measurements using X-rays with a suitable transmission mask should be broadly similar.

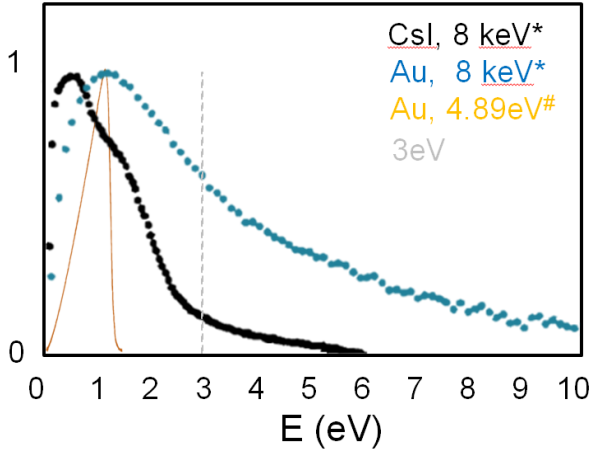


Figure 13. Electron energy distribution for CsI and Au excited at 8keV and Au at 4.89eV. Reproduced from J.Appl.Phys. **52**, 1509 (1981)^{14*} and J.Appl.Phys. **111**,124914 (2012)^{15#} with the permission of AIP Publishing

V. SPACE CHARGE EFFECTS

Space charge limits dynamic range in streak cameras when the temporal or spatial resolution elements expand due to coulomb repulsion. A small effect early in the tube can have a more significant effect compared to a stronger effect later in the tube as they have more time to expand. To establish where the most significant effects occur we performed end-to-end PIC simulations with space charge effects enabled for different regions in the tube. We divided the tube into the four regions identified in figure 2: i) the extraction region between the cathode and the mesh, ii) the focus region, iii) the crossover region at the anode aperture and iv) the drift region between the sweep plates and the detector. We simulated eleven electron sources equi-spaced 1.5mm along the photocathode. Each source comprised 10^6 electrons in a $50\mu\text{m} \times 50\mu\text{m}$ spot a 30ps Gaussian temporal profile and initial energy distribution corresponding to the Henke distribution for CsI. No ramp was applied to the sweep plates for this set of simulations. This simplification is justified by the simulations, which show little space charge effect in the drift region. The particle distribution at the detector shown qualitatively in figure 14 illustrates the relative contribution of the various regions to space charge blurring.

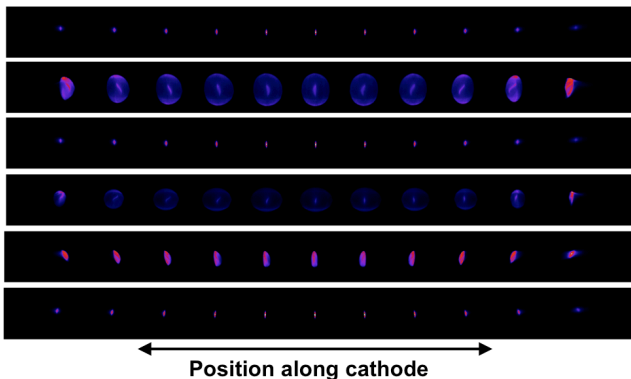


Figure 14 PIC simulated detector plane for 1.5mm spaced slotted mask source with space charge enabled from top to bottom for: i)

space charge off, ii) on throughout, iii) extraction region only, iv) crossover only, v) focus only, vi) drift only

The crossover and focus regions appear to contribute most to space charge blur. Surprisingly the extraction region alone contributes relatively little, considering the $\sim 100\text{ps}$ transit time across the gap starting at low energy. The significant contribution from the focus region is due to the relatively long time spent at roughly a third of the final tube potential, as can be seen in the color scale for figure 2.

VI. CONCLUSION

We have investigated two options for improving the spatial resolution of the NIF core diagnostics X-ray streak camera. The first using a mesh over the anode aperture leads to a significant reduction in Petzval field curvature but the blurring effect of the facet lenses associated with the mesh limits contrast $< 50\%$ above 10lp/mm. The second approach using a corrector lens element in a quasi-near-field region before the crossover, effectively eliminated Petzval field curvature, while maintaining spatial resolution out to the full aperture of the system. By detailed PIC modeling we have localized the regions of most significant space charge blurring to the anode aperture crossover. It is anticipated that with sufficient photocathode internal quantum efficiency (the number of secondary photoelectrons released per interacting X-ray) it may be possible to increase dynamic range by eliminating a fraction of the charge that would otherwise reach the crossover region. This assumes that we unambiguously detecting each event. As the number of electrons per interacting X-ray increases, the width of the distribution in the number collected will increase. We plan to quantify this noise source by making measurements on the statistic of secondary electron production and detection with and without a mesh at X-ray energies from 4.5keV to $\sim 70\text{keV}$ using filtered fluorescence from high Z targets excited by a 160keV X-ray tube.

The measurements described here were time integrated. We also need to examine the temporal modulation transfer function, although the existing time resolution is considered acceptable. To complete the picture we need to combine the effects of spatial and temporal MTF, internal and external QE of the cathode and statistics of the detector on the expected noise power spectrum in the signal as a function of space and time. We are refining the PIC simulation to provide a tool for convolving synthetic source data with the complete instrument function: Apply photocathode statistics to the time resolved spectrum from an atomic-hydro simulation to generate the source electrons for the PIC simulation of the camera, and finally apply detector statistics to the PIC output to get the synthetic streak record.

VII. ACKNOWLEDGMENTS

This work was performed under the auspices of the U.S. Department of Energy by Lawrence Livermore National Laboratory under Contract No. DE-AC52-07NA27344. IM release number #LLNL-CONF-694392

VIII. REFERENCES AND FOOTNOTES

- ¹J. D. Kilkenny, P. M. Bell, D. K. Bradley, D. L. Bleuel, J. A. Caggiano, E. L. Dewald, W. W. Hsing, D. H. Kalantar, R. L. Kauffman, D. J. Larson, *et. al.*, *The National Ignition Facility Diagnostic Set at the Completion of the National Ignition Campaign*, Fusion Science and Technology **69**,420 (2016)
- ²D. G. Hicks, B. K. Spears, D. G. Braun, R. E. Olson, C. M. Sorce, P. M. Celliers, G. W. Collins, O. L. Landen, *Streaked radiography measurements of convergent ablator performance (invited)*, Rev. Sci. Instrum. **81**(10), 10E304
- ³J. Hares, *Compact X-ray Streak Camera*, Rutherford Appleton Laboratory Report. Rutherford Appleton Laboratory, Didcot, England, Report No. RL-83-043, p. 1.33 (1983)
- ⁴*Handbook of Charges Particle Optics* 2nd Ed., Edited by Jon Orloff, p174 (CRC Press, Florida, 1983)
- ⁵O. Klemperer, W.D. Wright, Proc. Phys. Soc. **51** 296 (1936)
- ⁶D. Manura, D. Dahl. SIMION (R) 8.0 User Manual (Scientific Instrument Services, Inc. Ringoes, NJ 08551, <<http://simion.com/>>, January 2008)
- ⁷Computer Simulation Technology, AG Darmstadt, <http://www.cst.com/Content/Products/PS/Overview.aspx>
- ⁸*Time domain electromagnetic field computation with finite difference methods*, Weiland T, *International Journal of numerical modeling: electronic networks, devices and fields* **9** 295 (1996)
- ⁹M. Clemens, S. Drobny, H. Kruger, P. Pinder, O. Podebrad, B. Schillinger, B. Trapp, T. Weiland, M. Wilke, M. Bartsch, U. Becker and M. Zhang, *The electromagnetic simulation package MAFIA 4*, Proc. ICCEA'99 pp 565 – 568 (1999);
- ¹⁰V. K. Zworykin, G.A. Morton, *Applied Electron Optics*, J.Opt.Soc.Am **26**, 189 (1936)
- ¹¹H. Liebl, *Applied Charged Particle Optics*, pp18, (Springer-Verlag Berlin Heidelberg 2008)
- ¹²*Eagle V CCD camera*, Raptor Photonics Ltd., UK, <http://www.raptorphotonics.com/>
- ¹³H. Matsuda, L. Tóthb, F. Matsui, H. Daimon, *Evaluation of disturbing effect of mesh holes in wide-acceptance-angle electrostatic mesh lenses*, J. Electron. Spectrosc. Relat. Phenom. **195**, 78 (2014)
- ¹⁴B. L. Henke, J. P. Knauer, and K. Premaratne, *The characterization of x-ray photocathodes in the 0.1–10keV photon energy region*, J. Appl. Phys. **52**, 1509 (1981)
- ¹⁵G. Hechenblaikner, T. Ziegler, I. Biswas, C. Seibel, M. Schulze, N. Brandt, A. Schöll, P. Bergner, F. T. Reinert, *Energy distribution and quantum yield for photoemission from air-contaminated gold surfaces under UV illumination close to the threshold*, J.Appl.Phys. **111**, 124914 (2012)